IEEE Access
Multidisciplinary | Rapid Review | Open Access Journal

Received 19 December 2023, accepted 15 January 2024, date of publication 22 January 2024, date of current version 15 February 2024.

Digital Object Identifier 10.1109/ACCESS.2024.3357078

RESEARCH ARTICLE

Implementation of a Millimeter-Wave Butler Matrix on Metallic Nanowires-Filled Membrane Platform

BRUNO M. VERONA[1,2], ELIGIA SIMIONATO[3], (Student Member, IEEE), GUSTAVO PALOMINO[1], IVAN ALDAYA[3], (Member, IEEE), RAFAEL A. PENCHEL[3], (Member, IEEE), ARIANA L. C. SERRANO[1], (Member, IEEE), AND GUSTAVO P. REHDER[1]

[1]Laboratory of Microelectronics, Polytechnic School of the University of São Paulo (Poli-USP), São Paulo 05508-010, Brazil
[2]Micromanufacturing Laboratory, Institute for Technological Research (IPT), São Paulo 05508-901, Brazil
[3]School of Engineering, São Paulo State University (UNESP), São Paulo 01049-010, Brazil

Corresponding author: Ariana L. C. Serrano (aserrano@usp.br)

This work was supported in part by the Brazilian Agencies National Council for Scientific and Technological Development (CNPq) under Grant 409146/2021-8; and in part by the São Paulo Research Foundation (FAPESP) under Grant 2016/25779-9, Grant 2020/09889-4, Grant 2022/03519-6, and Grant 2022/08613-0.

ABSTRACT Wireless communications with greater transmission capacities are possible in the millimeter wave (mmWave) region. However, to overcome the significant propagation losses in this frequency band, it is necessary to employ more efficient and intelligent antennas based on MIMO and beam-steering phased array technologies. This paper demonstrates the fabrication of a beam steerable array antenna using a 4×4 Butler matrix at 60 GHz employing the metallic nanowire membrane (MnM) substrate. This substrate has the advantage of interconnecting two metallization layers by vias fabricated through its nanopores. Experimental characterization of the fabricated samples shows that the MnM platform represents a high-potential candidate for millimeter-wave front-ends supporting the beam-steering technique.

INDEX TERMS MnM plataform, Butler matrix, millimetre waves.

I. INTRODUCTION

The never-ending growth of global mobile data traffic has maintained an exponential increase in the last years [1]. For instance, from 2018 to 2022, the global mobile network data traffic increased from 26.6 to 90 exabytes (EB) per month and is projected to reach 325 EB per month in 2028 – a growth by a factor of nearly 400%. This tendency is expected to continue in the short and mid-term future, especially driven by the deployment of 5G systems, which has reached one billion users by the end of 2022 [1]. It is widely recognized that the sub-6 GHz band cannot further support the aforementioned data traffic demand, rendering it unattractive for the development of innovative technologies that are highly reliant on spectrum availability [2], [3], [4], [5], [6]. In this context, millimeter wave (mmWave) frequencies (30–300 GHz) have emerged as an interesting solution, since they are still largely unexploited for commercial wireless applications [7]. Therefore, various technologies are being proposed to operate within the under-utilized mmWave frequencies. For instance, the personal wireless communication operation mode of 5G operates between 52.6 and 71 GHz [8], whereas the evolution of the Wi-Fi family (802.11ad – WiGig) employs the frequency band around 60 GHz [7].

In addition to the extensively available bands, the adoption of mmWave bands presents two significant advantages: on the one hand, the larger wireless propagation loss provides higher immunity to interference and an improved security level, which is a critical requirement in modern wireless communication systems [9]. On the other hand, the shorter wavelength leads to more compact devices, including antennas. Consequently, mmWave technologies represent a high-potential solution to overcome the challenges not only of the near but also of middle future communication systems. However, these technologies' popularization and broad adoption will be possible only if the required devices

The associate editor coordinating the review of this manuscript and approving it for publication was Photos Vryonides.

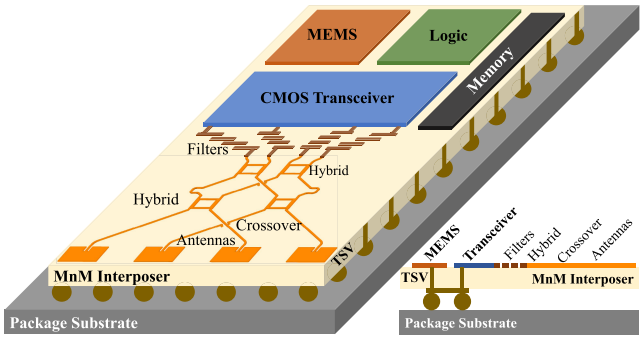

FIGURE 1. Illustration of a 3D heterogeneously integration System-on-Chip using MnM interposer and TSV of cooper nanowires.

can be efficiently manufactured. Therefore, a lot of effort has been dedicated to the development of cost-efficient manufacturing technologies for mmWave devices [10], [11], [12], [13], [14], [15].

In this sense, several semiconductor technologies have been developed for front-end implementation at mmWaves, among which it is worth mentioning: semiconductors of group III-V, bipolar silicon-germanium heterojunction transistor (SiGe), and bipolar CMOS (BiCMOS) or CMOS platforms in their multiple variants [10]. These technologies have matured significantly in recent years to enable the manufacture of active mmWave components with acceptable performance. CMOS transceivers, including those with integrated antennas, have already been demonstrated [11]. The 3D integration approach on silicon is interesting because it reduces interconnection losses, but implementing devices such as filters, couplers, phase shifters, impedance-matching networks, and especially array antennas, occupies a large area of the die, prohibitively increasing the final cost of the device [12].

Several alternatives have been proposed using interposers that enable the integration of active components manufactured with CMOS technology and passive components constructed in other platforms [12]. Fig. 1, for example, shows a complete transceiver on an interposer with an integrated circuit (IC) chip, an antenna, and interconnecting pins. The choice of materials, manufacturing technology, and integration techniques, however, is not trivial as it should attain a trade-off between cost and performance.

Alumina is well-known for its low loss at high frequencies, which allows high-performance devices [14]. Nevertheless, as a ceramic material, it is difficult to be holed, rendering the fabrication of vias difficult. Consequently, the adoption of alumina substrate limits the type of devices to be manufactured and their integration with other technologies. On the other hand, the use of alumina membrane, also denominated Metallic-Nanowire-Membrane (MnM), is a cost-efficient material made of anodic aluminum oxide (AAO) that inherits the isolation characteristics of the alumina but with patterned nanopores that can be exploited to build vias [13]. The nanopores, generated through an anodizing process of the alumina membrane, have diameter and spacing of the order of tens and hundreds of nanometers, respectively. The great differential of this technology is that, due to the nanopores, it enables the implementation of low-loss vertical nanowires by filling the nanopores with metal by electrodeposition, allowing the fabrication of low-loss Through-Substrate-Vias (TSVs) to interconnect the upper and bottom metallization layers [15]. Additionally, the alumina membrane provides a high dielectric constant ($\epsilon_r = 6.7$), enabling the development of smaller devices. The MnM platform has already demonstrated good performance in implementing high-quality transmission lines, TSVs, antennas, impedance transformers, and other passive devices [13]. Moreover, this substrate is capable of supporting slow-wave microstrip lines [17], [18], thus leading to the reduction of passive devices' footprint.

However, the performance of MnM in implementing more complex devices is still unclear. This is the case, for instance, of an array antenna equipped with a Butler matrix, which permits beam orientation without requiring active electrically controllable phase shifters. The implementation of the Butler matrix is particularly challenging due to the required crossovers and the sensitivity to the electrical path lengths.

In this work, we experimentally demonstrate that MnM is suitable for building sophisticated devices with accurate control of the electrical path lengths and high-performance crossovers. We will present a detailed description of the fabrication process using the MnM platform, as well as the evaluation of the technology's performance through the design, fabrication, and characterization of mmWave devices for operation in the 60 GHz band. In particular, we will also present microstrip lines and hybrid couplers that allow for the evaluation of the technology's capacity in relation to all three geometric dimensions (width, length, and thickness). Crossovers will be presented as a way of evaluating the capacity to fabricate TSVs. Finally, to evaluate the system integration, we will present the development of a complete Butler matrix, whose scheme is shown in Fig. 2.

The rest of the paper is organized as follows. In Section II, we describe the MnM fabrication process whereas the devices' development is presented in sections III through V. More specifically, Section III presents the hybrid coupler; Section IV describes the development of transmission lines and crossovers and the complete Butler matrix's project is detailed in Section V. Lastly, Section VI concludes this paper.

II. MNM FABRICATION PROCESS

The adopted MnM substrate is made of nanoporous alumina manufactured by Inredox through aluminum electrochemical oxidation and annealing at 600 °C for four hours. In particular, the employed MnM membrane manufactured, shown in Fig. 3(a), has a diameter of 25 mm and a thickness of 50 µm. The nanopores have a diameter of 40 nm and are spaced by 107 nm, which were measured using scanning electron microscopy. Once the MnM substrate is prepared,

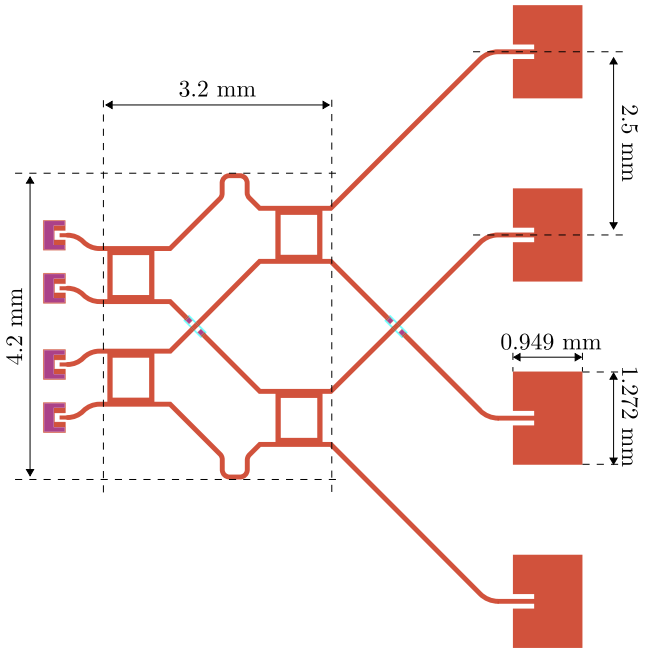

FIGURE 2. 4 × 4 Butler matrix layout with pads and patch antennas.

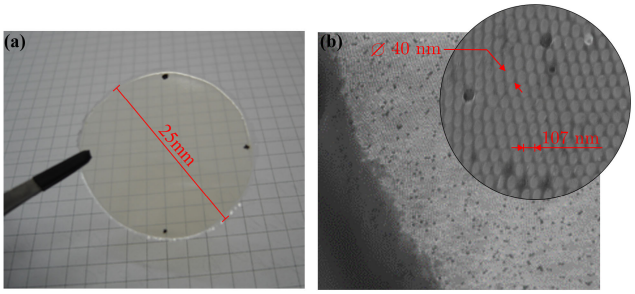

FIGURE 3. Inredox membrane: (a) picture of the whole membrane and (b) scanning electron microscopes image of the membrane nanopores.

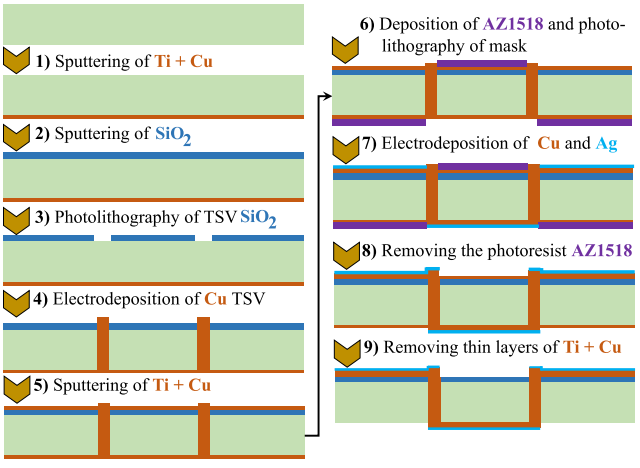

FIGURE 4. Manufacturing steps to build a device on MnM substrate, including a TSV.

the steps required to build the device are shown in Fig. 4 and are detailed below.

Step 1: Deposition of thin titanium (Ti, < 20 nm) and copper (Cu, < 50 nm) layers on the MnM subtract backside by RF magnetron sputtering (in orange, see Fig. 1). Titanium is used as an adherence layer for copper, which, in turn, is used as a seed layer for the electrodeposition of copper nanowires through the MnM pores;

Step 2: Deposition of a silicon dioxide (SiO_2, 200 nm) layer, by reactive sputtering on the MnM substrate front side (in blue, see Fig. 4). This layer is used as a mask to allow the selective growth of copper nanowires only in the regions of interest;

Step 3: Transfer of the TSV mask to the SiO_2 film by photolithography and etching with Buffered Oxide Etching (BOE);

Step 4: Growth of copper nanowires by electrodeposition in a cupric sulfate solution until a solid copper film is formed on the front side;

Step 5: Deposition of thin titanium and copper layers on the MnM substrate front side by RF magnetron sputtering;

Step 6: The devices and crossovers are defined using the photoresist AZ1518 on the front side of the membrane, and the thin copper is thickened up to 3 µm by electrodeposition. Soon after, the same process is realized on the membrane backside;

Step 7: Selective electrodeposition of copper (3 µm), is performed to thicken only the regions that are not masked by the photoresist;

Step 8: The photoresist on the front and back sides is removed;

Step 9: Remove the thin layers of copper and titanium using an etching process with a solution of ceric ammonium nitrate in acetic acid.

III. HYBRID COUPLER

One of the Butler matrix's fundamental building blocks is the quadrature hybrid coupler, illustrated in Fig. 5. It is a four-port network, composed of two pairs of transmission lines of impedances Z_0 and $Z_0/\sqrt{2}$ with lengths of $\lambda/4$. The ideal scattering matrix at the design frequency f_0 is given by [19]:

$$S^{HC} = \frac{-1}{\sqrt{2}} \begin{pmatrix} 0 & j & 1 & 0 \\ j & 0 & 0 & 1 \\ 1 & 0 & 0 & j \\ 0 & 1 & j & 0 \end{pmatrix} \quad (1)$$

The hybrid coupler design requires the optimization of the transmission lines' dimensions (widths and lengths) to achieve a scattering matrix as close as possible to (1). Even if a rough approximation of these parameters can be obtained through analytical expressions, these expressions do not consider some significant electromagnetic effects at the T-junctions [14]. Full-wave numerical solvers, such as Finite Element Method (FEM) available on the commercial software Ansys HFSS, are then used to refine the values of the dimensions that lead to the desired behavior.

The estimated initial dimensions for $\lambda/4$ at 60 GHz, $Z_0 = 50\ \Omega$ and $Z_0/\sqrt{2} = 35.35\ \Omega$ were obtained using Advanced Design System's (ADS) tool LineCalc, and are listed in Table 1. However, simulations revealed that these values lead

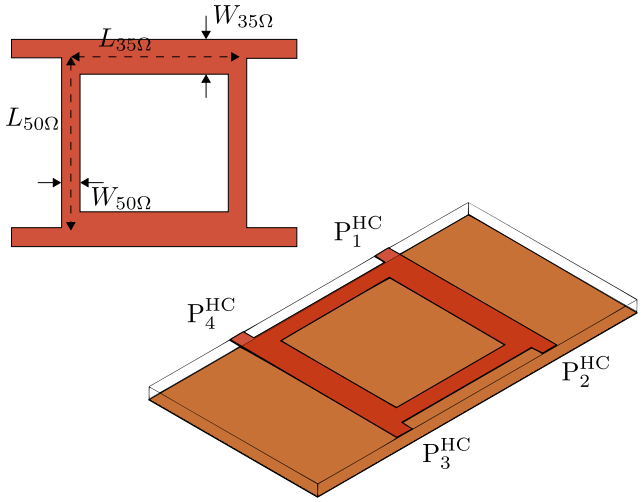

FIGURE 5. Top-view and perspective view of an integrated hybrid coupler, indicating the dimension parameters and the port identification.

TABLE 1. Dimensions of the hybrid coupler before and after optimization.

	$W_{50\Omega}$	$L_{50\Omega}$	$W_{35\Omega}$	$L_{35\Omega}$
Initial values	66 µm	575 µm	120 µm	556 µm
Optimized values	72 µm	545 µm	123 µm	570 µm

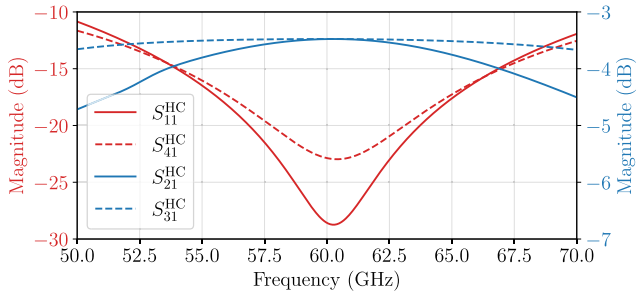

FIGURE 6. Magnitude of the S_{11}, S_{21}, S_{31}, and S_{41} of the hybrid coupler (simulated results).

to an unbalance between the outputs and a frequency shift of the impedance matching point. The analytically estimated dimensions were refined by performing a parametric analysis of the four variables using the aforementioned software in which the MnM was modeled as a 50 µm-thick solid substrate with $\epsilon_r = 6.7$, $\tan\delta = 0.015$ and the metallic layers were modeled with a thickness of 3 µm and conductivity of $5.8 \cdot 10^7$ S/m (copper) [17]. The restrictions in the lithography process during the fabrication were considered by setting a resolution of 1 µm during the optimization process. The optimized dimensions, also presented in Table 1, resulted in a hybrid coupler device whose behavior in terms of scattering parameters was obtained from a simulation utilizing Ansys HFSS, and is shown in Fig. 6.

Two samples of the optimized hybrid coupler were fabricated and characterized. One of the samples is shown in Fig. 7. Measurements were performed using a Keysight PNA N5227B vector network analyzer (VNA); MPI Titan ground-signal-ground (GSG) probes, with a 100 µm pitch; and a

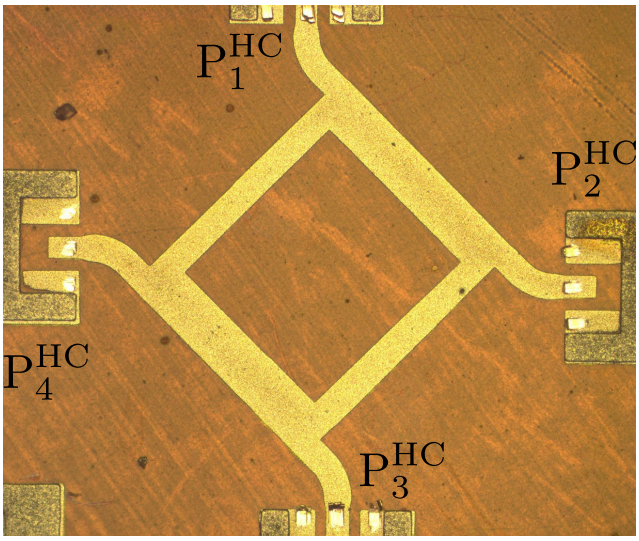

FIGURE 7. Photograph of the fabricated hybrid couplers.

line-reflect-reflect-match (LRRM) calibration. The couplers' response curves in Fig. 8 show (a) the magnitude of the S_{11} and S_{41}, (b) the magnitude of the S_{21} and S_{31}, and (c) the phase difference between S_{21} and S_{31} for both samples. At the design frequency of 60 GHz, insertion loss and coupling were 3.6 dB and 3.9 dB, respectively. Thus, the measured unbalance was lower than 0.3 dB for the two samples. The reflection coefficient of both samples remained below –15 dB for a 10 GHz wide band, while isolation was higher than 20 dB over a 5-GHz-wide band around the design frequency. The phase difference between the outputs at 60 GHz was 90.8° and remained in the interval from 87° to 93° in the range of 54-63 GHz.

IV. TSV-BASED CROSSOVER

As already mentioned, one of the advantages of the MnM substrate is the potential to create compact and low insertion loss TSVs employing a simple fabrication process (detailed in Section II) [15]. However, there is no precise analytical model capable of predicting the losses and possible mismatches caused by the vias. Due to the complexity of the nanowire structure that constitutes the vias (size, aspect ratio, density, etc.), the discretization and solution of Maxwell's equations in this domain would require prohibitively high computational resources. For this reason, we chose not to use simulation tools to design and optimize the TSVs, but rather create layouts of simple structures with dimensions compatible with transmission lines and other components used in the Butler matrix (detailed in Section V). Afterward, the electrical parameters of interest would be extracted to analyze possible losses and parasitic characteristics.

Considering that the interconnections between the Butler matrix's components were done with 50 Ω microstrip lines, the crossover between two lines was implemented as a detour of one of them to a 50 Ω co-planar waveguide (CPW) section in the bottom metallization level, as shown in Fig. 9. The

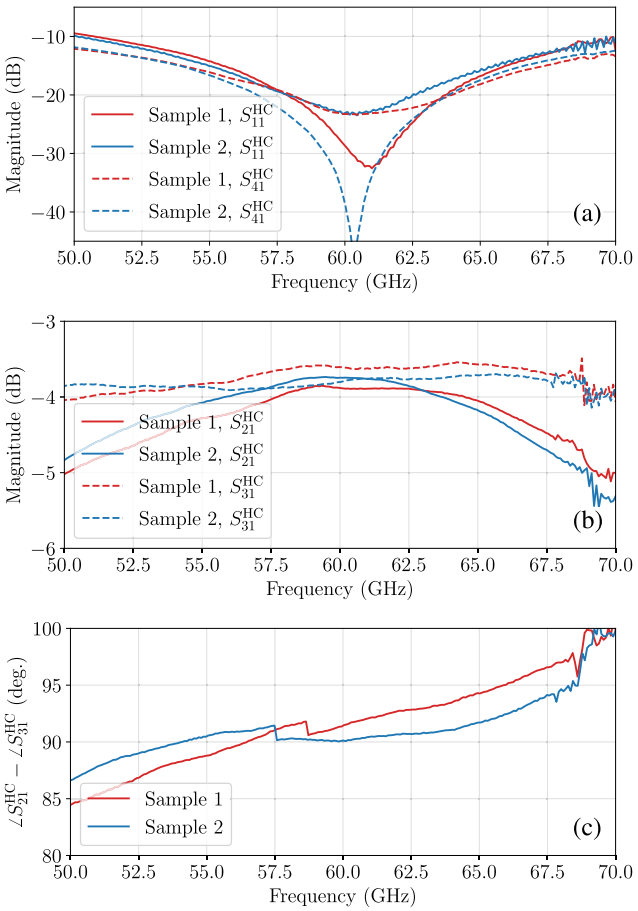

FIGURE 8. Characterization of the two fabricated samples of hybrid couplers: (a) the magnitude of the S_{11} and S_{41}, (b) the magnitude of the S_{21} and S_{31}, and (c) the phase difference between S_{21} and S_{31}.

lines' width and the slot in the bottom metallization level were dimensioned so that both the microstrip and CPW section had an impedance of 50 Ω. The length of the CPW section had to be sufficiently small for a compact device, yet large enough to prevent crosstalk between the direct microstrip section and the microstrip with vias and CPW section. In order to attain a trade-off between compactness and performance, three crossover configurations with different CPW section lengths were fabricated. The layouts of the fabricated crossovers are shown in Fig. 10. Additionally, the layout includes transmission lines with vias and a CPW section, and a section of microstrip without vias used as a reference for losses and phase shifting, both separated from the crossovers (see Fig. 10). Fig. 11 exhibits one sample of the 300 µm CPW crossover and the reference microstrip line as seen through an optical microscope.

In Fig. 12, $|S_{11}|$ and $|S_{21}|$ curves for the 300 µm and 400 µm CPW sections with vias are shown together with those of the reference microstrip line. The results show that the signal detour to a CPW in the bottom metallization level does not significantly impact insertion losses, showing a penalty lower than 0.1 dB at 60 GHz compared to the reference microstrip. These slight discrepancies may be attributed to random

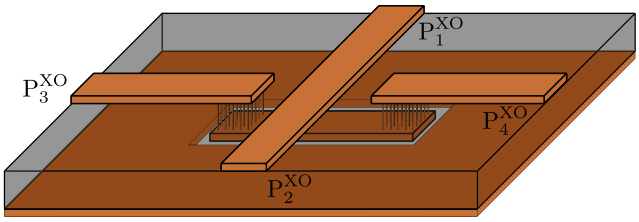

FIGURE 9. 3D view of the crossover structure.

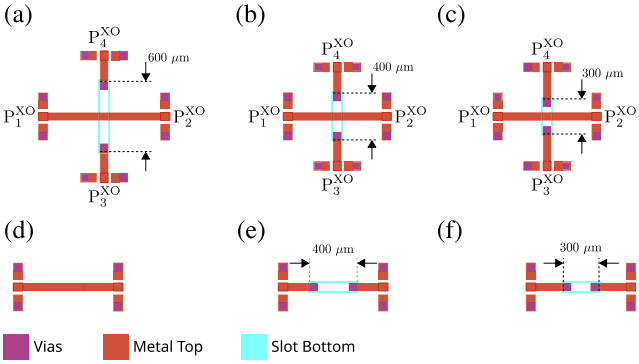

FIGURE 10. Layouts of the crossovers with CPW section lengths of (a) 600 µm, (b) 400 µm, and (c) 300 µm, a (d) section of microstrip line for reference, and transmission lines with CPW section lengths of (e) 400 µm and (f) 300 µm.

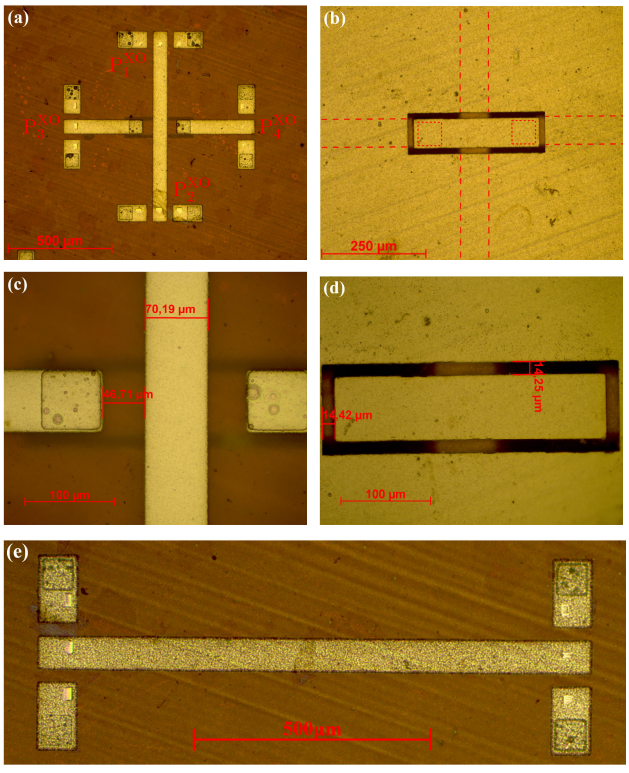

FIGURE 11. Optical microscopy images of the fabricated samples: (a) front and (b) back view of the crossover with 300 µm CPW; (c) front and (d) back view of the crossover with scale 1:100 µm; (e) reference microstrip line.

environmental errors during the measurement process, but they are so small that can also fall within the equipment error. Observing the phase, however, different behavior is

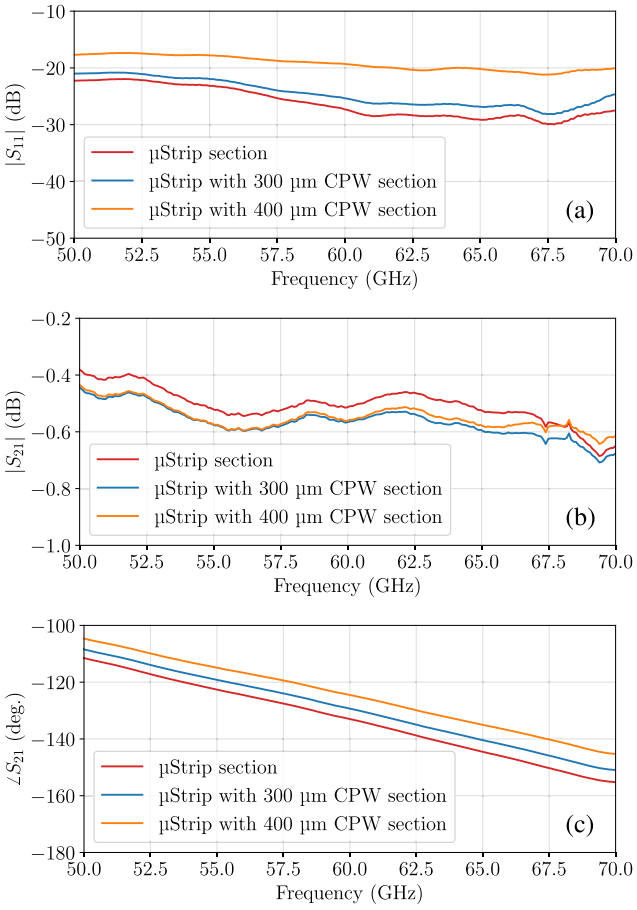

FIGURE 12. Measurements of (a) $|S_{11}|$, (b) $|S_{21}|$ and (c) phase ($\angle S_{21}$) of 300 µm, 400 µm CPW section with vias and reference microstrip line.

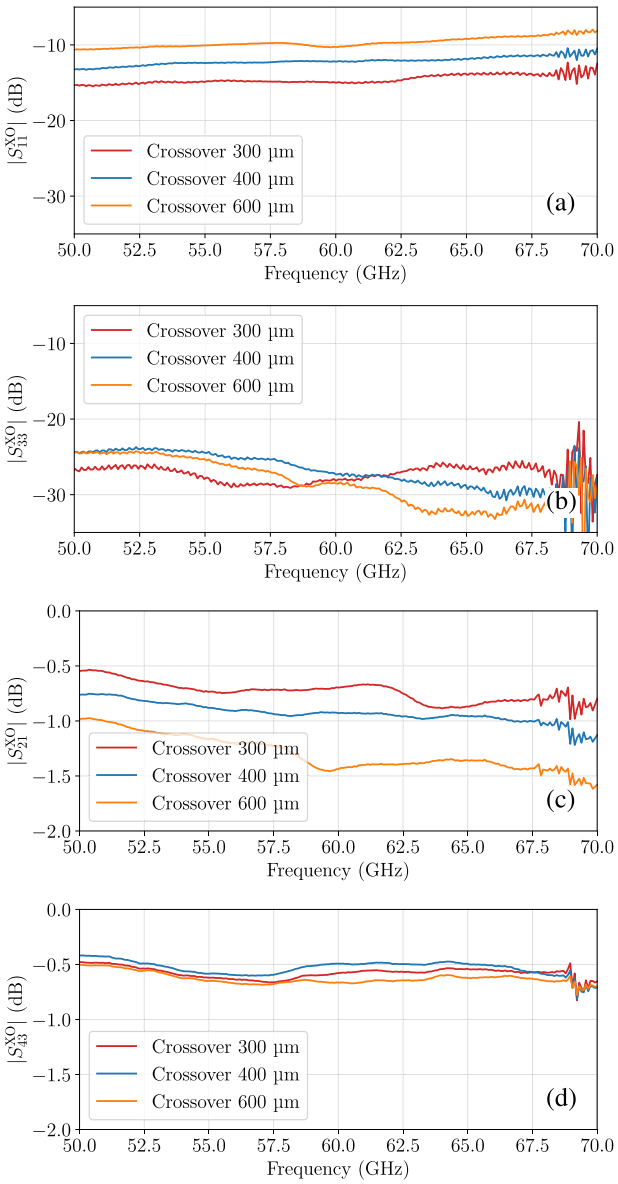

FIGURE 13. Characterization of the fabricated crossovers' reflection coefficient of (a) the direct section and the (b) the section with CPW; transmission coefficient of (c) the direct section, and (d) section with CPW.

noted. Although the dimensions of both microstrip and CPW sections were adjusted so that the characteristic impedance is close to 50 Ω, the propagation constants differ. Therefore, the longer the CPW segment, the more distinct the difference presented between the behavior of the structures with vias and CPW section, and the reference microstrip line. This may be observed in the phase graph in Fig. 12, which shows that the structures with vias and 300 µm and 400 µm CPW sections deviate 4.8° and 8.5° from the reference microstrip line at 60 GHz, respectively.

The scattering parameters of the fabricated crossovers are presented in Fig. 13, where we show (a-b) the reflection coefficients and (c-d) transmission coefficients of the direct as well as the CPW and vias sections. At 60 GHz, the section with vias presented a reflection coefficient below –25 dB and insertion losses between 0.5 dB and 0.7 dB for all three manufactured structures. The direct section, however, exhibited higher losses and poorer matching, in addition to more significant performance degradation as the CPW segment's length grew. This performance degradation of the direct microstrip section can be attributed primarily to the slot in the bottom metallization layer, designed to correspond to a 50 Ω CPW line. In the direct section, the slot functions as a defected ground structure (DGS), which disrupts the current distribution of the ground plane. Consequently, it alters the effective resistance, capacitance, and inductance of the microstrip line by introducing resistance, capacitance, and inductance associated with the slot [20].

To verify the influence of the slot on the degradation of the microstrip line's performance, we conducted simulations that exclusively considered the microstrip's direct section and the slot in the bottom metallization layer, functioning as a DGS. The slot's length was examined at 300 µm, 400 µm, and 600 µm, to match the analysis performed for the crossover. Figure 14 illustrates (a) the reflection coefficients and (b) transmission coefficients obtained from the simulations, demonstrating poorer matching and higher losses as the slot length grows, which is consistent with

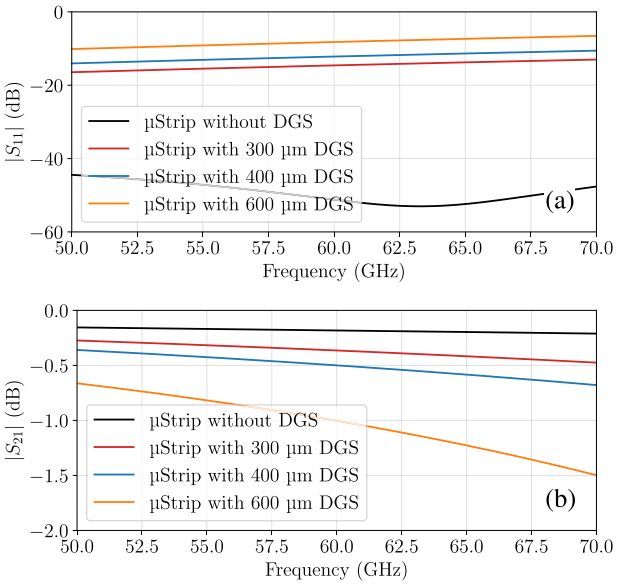

FIGURE 14. Simulated results of the magnitudes of (a) reflection coefficient and (b) transmission coefficient for a microstrip section with a slot (DGS) on the ground plane corresponding to the CPW section.

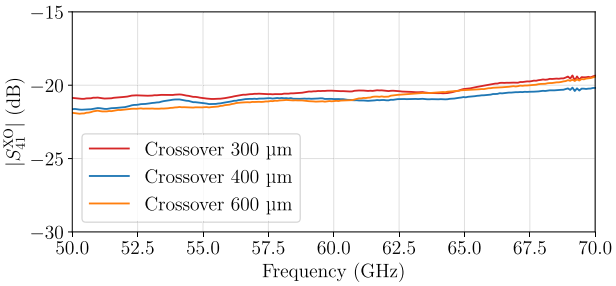

FIGURE 15. Measured isolation of the fabricated crossovers.

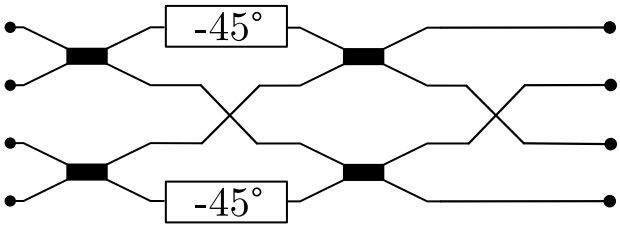

FIGURE 16. Schematic of a 4 × 4 Butler matrix.

TABLE 2. 4 × 4 Butler matrix progressive phase difference and the resulting beam direction.

Input port	Phase difference at outputs	Beam direction*
1	$\Delta\psi_1 = -45°$	$\theta_{BS,1} = -14.48°$
2	$\Delta\psi_2 = +135°$	$\theta_{BS,2} = +48.59°$
3	$\Delta\psi_3 = -135°$	$\theta_{BS,3} = -48.59°$
4	$\Delta\psi_4 = +45°$	$\theta_{BS,4} = +14.48°$

* With respect to broadside

the observations made for the crossover in Fig. 13. For the crossover design, the slot's length is the sole controllable variable, as the other dimensions of the slot are fixed to achieve a 50 Ω CPW line. Thus, we established the crossover design by evaluating the outcomes presented in Fig. 13. The best case was the crossover with a 300 µm CPW section, for which the reflection and transmission coefficients at 60 GHz were –15 dB and 0.7 dB, respectively. At this frequency, the crossover with a 600 µm CPW section presented an insertion loss higher than 1.4 dB and a reflection coefficient of around –10.2 dB.

Another relevant aspect for evaluating the crossovers is the isolation between the two lines, which quantifies the signal interference between the direct microstrip line and the one with CPW sections and vias. Although both sections are electrically isolated, a capacitive coupling between the two lines leads to a signal leak that increases with frequency. This effect can be seen in the curves in Fig. 15, where the measured isolation levels for the three crossover structures are shown. In Fig. 15, we can also observe that even though signal crossing increases at higher frequencies, at 60 GHz isolation still exceeds 20 dB for all crossover structures. Additionally, we can note an increase in signal interference for the more compact crossover structures. However, even for the 300 µm crossover, the most compact fabricated device, the isolation level obtained is acceptable for application in the Butler matrix. All measurements of the crossover were acquired using the same setup described in Section III.

V. DESIGN AND FABRICATION OF THE BUTLER MATRIX

The Butler matrix is a linear and passive network with typically N inputs and N outputs, composed of an arrangement of hybrid couplers, crossovers, and fixed phase shifters. The signal injected into one of the input ports of the Butler matrix is equally split among the output ports with a progressive phase. The phase difference value will change depending on the input port at which the signal is input. In this way, by feeding the elements of an array antenna with a Butler matrix, whose inputs are selectively excited using an RF switch, the beam direction can be controlled. The schematic of a 4 × 4 Butler matrix designed according to the method proposed in [21] is presented in Fig. 16.

A 4 × 4 Butler matrix provides consecutive phase differences of $\Delta\psi_1 = -45°$, $\Delta\psi_2 = +135°$, $\Delta\psi_3 = -135°$ or $\Delta\psi_4 = +45°$, depending on the excited input port. With these phase differences, the beam-steering angle is given by:

$$\theta_{BSi} = \arcsin\left(\frac{\Delta\psi_i \lambda}{2\pi d}\right), \text{ with } i \in [1, \ldots, 4], \qquad (2)$$

where λ is the operation wavelength and d is the center-to-center element separation.

If this network is connected to a linear array of antennas spaced by a distance $d = \lambda/2$, the angle of the main beam can be oriented toward $\theta_{BS} = \pm 14.48°$ and $\theta_{BS} = \pm 48.59°$ with respect to the broadside direction. The progressive phase difference and the resultant beam direction in terms of the exited input port are summarized in Table 2.

We combined the devices described in previous sections according to the schematic presented in [21] to build the first complete 4×4 Butler matrix on MnM technology. In addition, to verify that the implemented Butler matrix induces the

TABLE 3. Transmission coefficients and phase differences at the outputs of the matrix simulated using MoM.

	Transmission coefficients (dB)					Phase differences (deg.)				
n	$\lvert S_{5n}\rvert$	$\lvert S_{6n}\rvert$	$\lvert S_{7n}\rvert$	$\lvert S_{8n}\rvert$	$\overline{S} \pm \sigma$	$\Delta\psi_{n,\text{ideal}}$	$\angle S_{6n} - \angle S_{5n}$	$\angle S_{7n} - \angle S_{6n}$	$\angle S_{8n} - \angle S_{7n}$	$\lvert\text{error}\rvert_{\max}$
1	-7.6	-7.4	-9.5	-7.9	-8.02 ± 0.39	-45	-43.8	-30.5	-57.6	14.5
2	-8.6	-9.2	-6.6	-8.0	-8.09 ± 1.19	135	114.9	141.4	144.5	20.1
3	-7.9	-6.8	-9.2	-8.6	-8.20 ± 1.40	-135	-143.5	-134.2	-112.6	22.4
4	-8.0	-9.0	-7.4	-7.7	-8.06 ± 0.40	45	57.6	38.4	42.7	12.6

TABLE 4. Transmission coefficients and phase differences at the outputs of the matrix simulated in the SPICE environment using measured S parameters.

	Transmission coefficients (dB)					Phase differences (deg.)				
n	$\lvert S_{5n}\rvert$	$\lvert S_{6n}\rvert$	$\lvert S_{7n}\rvert$	$\lvert S_{8n}\rvert$	$\overline{S} \pm \sigma$	$\Delta\psi_{n,\text{ideal}}$	$\angle S_{6n} - \angle S_{5n}$	$\angle S_{7n} - \angle S_{6n}$	$\angle S_{8n} - \angle S_{7n}$	$\lvert\text{error}\rvert_{\max}$
1	-8.7	-8.6	-8.8	-8.9	-8.89 ± 0.10	-45	-45.0	-41.3	-44.8	3.7
2	-8.9	-8.5	-8.8	-8.7	-8.78 ± 0.20	135	134.0	140.0	134.5	5.0
3	-8.7	-9.0	-8.5	-8.8	-8.77 ± 0.13	-135	-136.9	-130.6	-136.1	4.4
4	-8.8	-8.7	-8.6	-8.5	-8.81 ± 0.14	45	42.1	51.6	42.3	6.6

required progressive phase, we connected the Butler matrix to a 4-element array antenna, which allowed us to validate the beam steering capability of the fabricated Butler matrix. The characterization of the components presented in Sections III and IV was used to design and predict the performance of the Butler matrix, which was simulated using Momentum from ADS that employs the Method of Moments (MoM). The 4×4 Butler matrix layout, based on Fig. 16, is shown in Fig. 17. This layout was designed to operate at 60 GHz and feed a four-element linear array of patch antennas with an interelement separation of $\lambda/2 \approx 2.5$ mm.

The layout was composed of five stages that were built using the previously designed and characterized devices, except for the 45° phase shifter, which was designed according to the available space between stages 2 and 4 (see Fig. 17). To position the devices in the matrix layout, the hybrid couplers were fixed so that the crossing of two transmission lines would always occur orthogonally, in order to make the design compatible with the crossover that was already designed. In addition, the device was designed to ensure that the distances between each input and the four outputs to be the same, thus avoiding unwanted phase differences. The couplers and crossovers were positioned and interconnected, and the 45° phase shifters in stage 3 were designed, using the 774 µm straight lines as reference. A curved microstrip section was used to design the 45° phase shifter which resulted in a 1095 µm long microstrip line, as shown in Fig. 17.

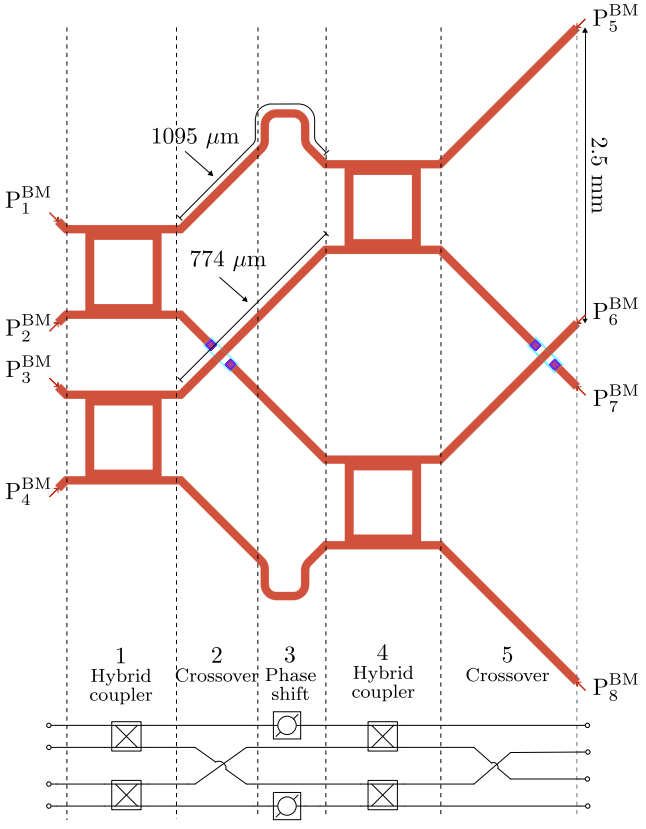

FIGURE 17. 4 × 4 Butler matrix layout.

In order to obtain a first prediction of the assembled Butler matrix's behavior, we analyzed the results obtained from two different simulation methods: MoM, and SPICE with measured data obtained from the characterization of the couplers, crossovers, and transmission lines. Simulations using MoM considered the top and bottom metal layers as bidimensional planar conductors, with sheet resistance equivalent to a 3 µm thick layer of copper ($\sigma_{\text{copper}} = 5.8 \cdot 10^7$ S/m). The Tables 3 and 4 compile the main results obtained at 60 GHz for the simulations using MoM, and using data from two measured samples. Comparing the results from the two simulation procedures, the behavior predicted by the SPICE environment, using measured data from fabricated sample (tables 3 and 4) indicate that the proposed layout is close to the ideal model of the Butler matrix, with progressive phase shifts and uniform power between outputs. On the other hand, simulations using MoM (Table 3) revealed an

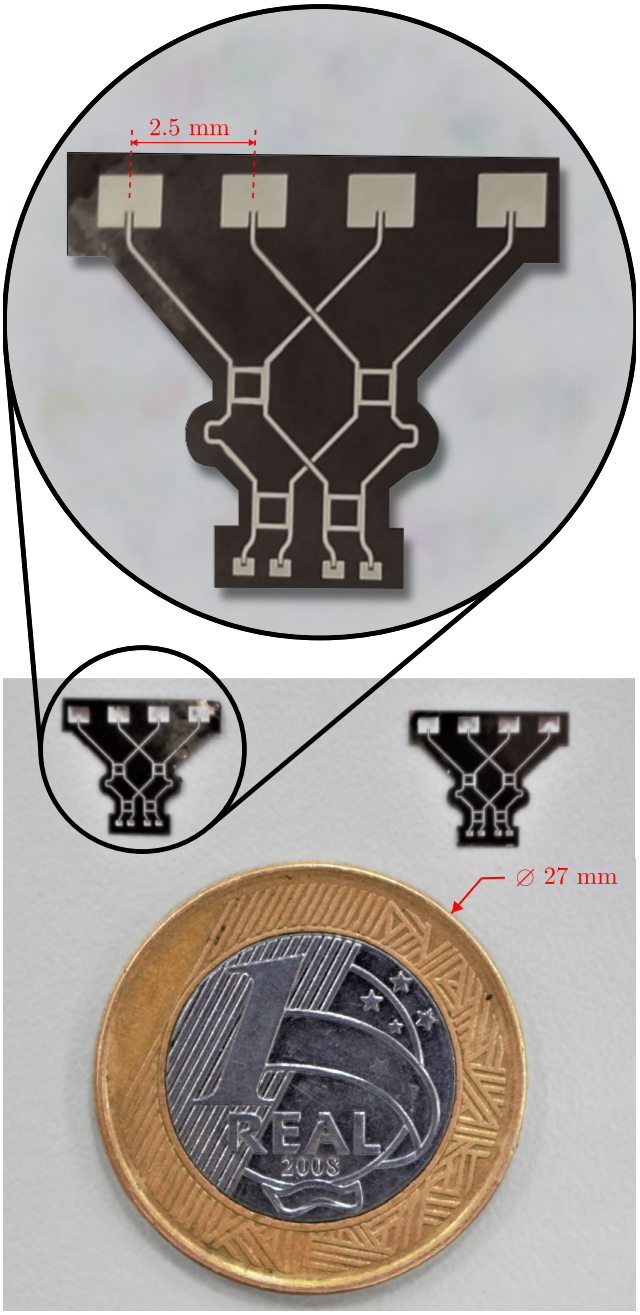

FIGURE 18. Fabricated 4 × 4 Butler matrix.

inferior performance with more dispersed phase differences and less uniform power distribution at the outputs but still indicating that the proposed layout is able to produce the desired behavior for a Butler matrix.

With the design of the 4×4 Butler matrix done, we created the layout for the complete device, shown in Fig. 2, including the RF pads at the inputs and the patch antenna array. The dimensions for the patch antennas are such that allow the operation at the V band (57 GHz to 66 GHz). To analyze the designed device's ability to control the beam direction radiated by the antenna array, the final layout (Fig, 2) was imported into ADS' Momentum environment for numerical

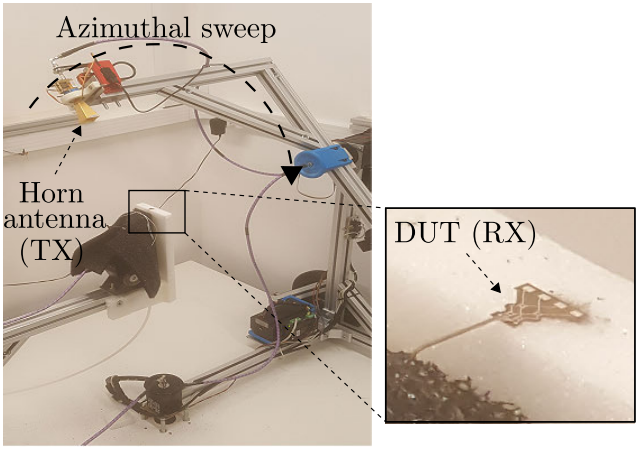

FIGURE 19. Setup used to measure the radiation patttern.

simulation. The device's operation at 60 GHz was evaluated using the same parameters employed for the simulation of the Butler matrix layout of Fig. 17.

Using the layout shown in Fig. 2, a sample with two complete 4 × 4 Butler matrices, shown in Fig. 18, was fabricated according to the process detailed in Section II. The individual matrices were separated using a laser cutting system (LPKF U3). The samples were characterization by measuring the radiation pattern of the 4-element array antenna when each matrix input is excited. To do that, we used the test setup shown in Fig. 19, where a horn antenna is fixed to a movable structure that is able to conduct the azimuthal sweep around the device under test (DUT) [16]. With this setup, each radiation pattern was measured by positioning the RF probe (connected to the VNA) in one of the Butler matrix inputs while the remaining inputs were kept open. Nonetheless, even with three unmatched inputs, the reflection coefficient for the excited input in each of the four measurements remained lower than −10 dB for the expected operation bandwidth.

Fig. 20(a) presents the four simulated radiation patterns. For each of them, one of the input ports is excited, while the others remain matched, with null incident power. The simulated radiation patterns predict that the designed Butler matrix is able to steer the antenna array's radiation pattern with reasonable agreement with the ideal angles. Even with eventual phase errors and mismatches predicted in the designed layout, the ideal directions of $\pm 14,5°$ and $\pm 48,6°$ are within the half-power beam width (HPBW). Furthermore, the side lobe level (SLL) is affected by beam steering, with wider angles of beam-steering resulting in higher SLL. Fig. 20(a) shows that the SLL is −12 dB when power is applied to ports 1 and 4, while for ports 2 and 3 the SLL rose up to −6.9 dB. The measured beam directions are shown in Fig. 20(b) and compiled in Table 5. From the values organized in Table 5, it is possible to observe in agreement with the simulation results, the measured angles are within HPBW.

Measurements of the reflection coefficient for each input port of the Butler matrix are presented in Fig. 21. It can be

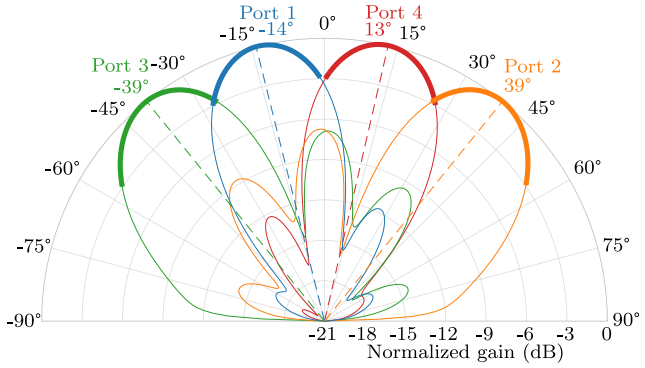

(a) MoM simulation

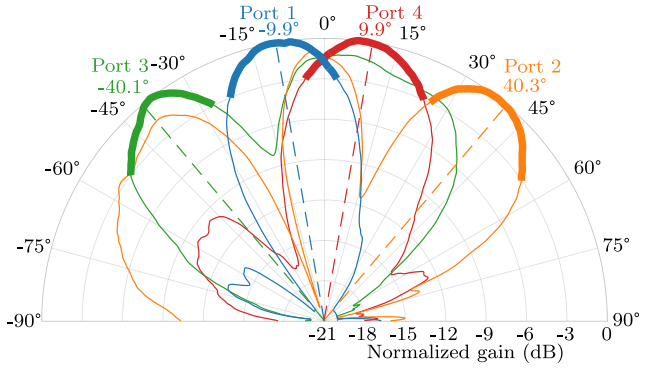

(b) Measurement

FIGURE 20. Radiations patterns at 60 GHz for 4 × 4 Butler matrices connected to an antenna array.

TABLE 5. Beam directions* observed in each fabricated sample of the Butler matrix.

	$\theta_{BS,1}$	$\theta_{BS,2}$	$\theta_{BS,3}$	$\theta_{BS,4}$
Measurement	-9.9°	+40.3°	-40.1°	+9.9°
Ideal	-14.5°	+48.6°	-48.6°	14.5°

* Referenced at broadside

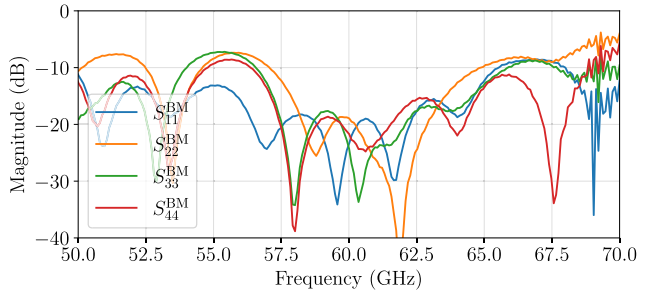

FIGURE 21. Measured reflection coefficient for each of the Butler matrix's input port.

observed that the matrix is operational within the 57.5 GHz to 65 GHz range. However, when examining the gain as a function of frequency (see Fig. 22), it becomes apparent that the gain is not constant across the entire operational bandwidth; instead, it remains relatively stable within a narrow bandwidth around 60 GHz. Fig. 22 also illustrates that when the matrix feeds only one antenna, as in this project, the gain is not substantial. Therefore, additional antennas may be incorporated into the array to enhance directivity and, consequently, the gain.

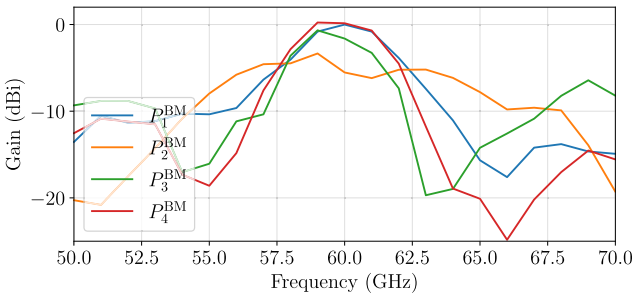

FIGURE 22. Measurements of gain as a function of frequency for each input port of the Butler matrix.

TABLE 6. Comparison between the proposed Butler matrix and the matrices presented in literature operating at millimeter waves.

Ref.	f_0 (GHz)	BW (%)	Tech.	Size (λ_0^2)	Type
[23]	70	28.6	MWG	9 × 6	4 × 8
[24]	70	14.3	SIW	Not reported	4 × 4
[25]	79	10.7	Finline	Not reported	4 × 4
[26]	60	6.5	MWG	17.7 × 7.1	4 × 4
[27]	60	10.7	MWG	28 × 9.8	8 × 8
[28]	76	15.8	Duroid 6002	26.1 × 4.3	5 × 5
[22]	61	16.4	CMOS	0.29 × 0.19	8 × 8
This work	**60**	**12.2**	**MnM**	**0.84 × 0.64**	**4 × 4**

f_0: central frequency, BW: bandwidth, MWG: metallic waveguide, SIW: substrate integrated waveguide.

A comparison between this work and other Butler matrices operating at millimeter waves reported in the literature is presented in Table 6. The proposed 4 × 4 Butler matrix, fabricated on the MnM platform, exhibits the smallest footprints, aside from the design presented in [22], which employs CMOS technology. However, the matrix in [22] is a multi-layered structure, unlike the single-layer fabrication process used in this work, rendering the proposed Butler matrix simpler to manufacture.

VI. CONCLUSION

In this work we have presented the design, fabrication, and characterization of transmission lines, crossovers, and couplers using the MnM platform. The individual devices were then used to build a complete Butler matrix, which demonstrated the capabilities of the MnM platform in functioning as an interposer for system integration.

The adopted fabrication method was able to produce vias capable of interconnecting the bottom and top metallization layers, thus enabling the construction of non-planar devices. These vias were then used to implement high-performance crossover. Experimental results reveal that the insertion loss, isolation, and reflection levels of constructed crossovers are sufficient to build an operational 4 × 4 Butler matrix. The fabricated couplers showed low reflection losses, good isolation, and output signals that are approximately balanced and in quadrature at 60 GHz. Lastly, this work enabled the fabrication and characterization of an initial prototype, utilizing the MnM platform, of the Butler matrix feeding a linear array antenna, capable of modifying the beam direction according to the matrix's input.

Consequently, the results presented in this work contribute to developing a complete cost-efficient RF front-end on the MnM substrate, which enables facilitated integration with active components manufactured utilizing well-established technologies such as CMOS. Additionally, by offering an RF front-end that supports the beam-steering technique, it is expected that the proposed design can be exploited for various applications at millimeter wave frequencies, particularly in the advancement of technologies such as 60 GHz Wi-Fi.

REFERENCES

[1] (Nov. 22, 2022). *Ericsson Mobility Report Thing's Credible!, Blog*. [Online]. Available: https://www.ericsson.com/en/reports-and-papers/mobility-report/reports/november-2022
[2] L. Wei, R. Q. Hu, Y. Qian, and G. Wu, "Key elements to enable millimeter wave communications for 5G wireless systems," *IEEE Wireless Commun.*, vol. 21, no. 6, pp. 136–143, Dec. 2014.
[3] M. Marcus and B. Pattan, "Millimeter wave propagation: Spectrum management implications," *IEEE Microw. Mag.*, vol. 6, no. 2, pp. 54–62, Jun. 2005.
[4] J. Ma, R. Shrestha, L. Moeller, and D. M. Mittleman, "Invited article: Channel performance for indoor and outdoor terahertz wireless links," *APL Photon.*, vol. 3, no. 5, Feb. 2018, Art. no. 051601.
[5] T. S. Rappaport, Y. Xing, G. R. MacCartney, A. F. Molisch, E. Mellios, and J. Zhang, "Overview of millimeter wave communications for fifth-generation (5G) wireless networks—With a focus on propagation models," *IEEE Trans. Antennas Propag.*, vol. 65, no. 12, pp. 6213–6230, Dec. 2017.
[6] J. Wells, "Faster than fiber: The future of multi-G/s wireless," *IEEE Microw. Mag.*, vol. 10, no. 3, pp. 104–112, May 2009.
[7] Z. Pi and F. Khan, "An introduction to millimeter-wave mobile broadband systems," *IEEE Commun. Mag.*, vol. 49, no. 6, pp. 101–107, Jun. 2011.
[8] 3GPP. (2023). *3rd Generation Partnership Project (3GPP) Release 17 Specifications*. [Online]. Available: https://www.3gpp.org/specifications-technologies/releases/release-17
[9] C. H. Doan, S. Emami, D. A. Sobel, A. M. Niknejad, and R. W. Brodersen, "Design considerations for 60 GHz CMOS radios," *IEEE Commun. Mag.*, vol. 42, no. 12, pp. 132–140, Dec. 2004.
[10] A. Scavennec, M. Sokolich, and Y. Baeyens, "Semiconductor technologies for higher frequencies," *IEEE Microw. Mag.*, vol. 10, no. 2, pp. 77–87, Apr. 2009.
[11] F. Lin, J. Brinkhoff, K. Kang, D. D. Pham, and X. Yuan, "A low power 60 GHz OOK transceiver system in 90 nm CMOS with innovative on-chip AMC antenna," in *Proc. IEEE Asian Solid-State Circuits Conf.*, 2009, pp. 349–352.
[12] O. E. Bouayadi, L. Dussopt, Y. Lamy, C. Dehos, C. Ferrandon, A. Siligaris, B. Soulier, G. Simon, and P. Vincent, "Silicon interposer: A versatile platform towards full-3D integration of wireless systems at millimeter-wave frequencies," in *Proc. IEEE 65th Electron. Compon. Technol. Conf. (ECTC)*, May 2015, pp. 973–980.
[13] M. V. Pelegrini, J. M. Pinheiro, L. G. Gomes, G. P. Rehder, A. L. C. Serrano, F. Podevin, and P. Ferrari, "Interposer based on metallic-nanowire-membrane (MnM) for mm-wave applications," in *Proc. 11th Eur. Microw. Integr. Circuits Conf. (EuMIC)*, 2016, pp. 532–535.
[14] M. Bertrand, G. P. Rehder, A. L. C. Serrano, L. G. Gomes, J. M. Pinheiro, R. C. A. Alvarenga, N. Kabbani, D. Kaddour, V. Puyal, E. Pistono, and P. Ferrari, "Integrated waveguides in nanoporous alumina membrane for millimeter-wave interposer," *IEEE Microw. Wireless Compon. Lett.*, vol. 29, no. 2, pp. 83–85, Feb. 2019.
[15] J. M. Pinheiro, M. V. Pelegrini, L. Amorese, P. Ferrari, G. P. Rehder, and A. L. C. Serrano, "Nanowire-based through substrate via for millimeter-wave frequencies," in *IEEE MTT-S Int. Microw. Symp. Dig.*, 2016, pp. 1–4.
[16] J. E. G. Lé, M. Ouvrier-Buffet, L. G. Gomes, R. A. Penchel, A. L. C. Serrano, and G. P. Rehder, "Integrated antennas on MnM interposer for the 60 GHz band," *J. Microw., Optoelectronics Electromagn. Appl.*, vol. 21, no. 1, pp. 184–193, Mar. 2022. [Online]. Available: http://www.scielo.br/j/jmoea/a/Zm95w4WLFKVYp3cmZGjPJQJ/
[17] A. L. C. Serrano, A.-L. Franc, D. P. Assis, F. Podevin, G. P. Rehder, N. Corrao, and P. Ferrari, "Modeling and characterization of slow-wave microstrip lines on metallic-nanowire-filled-membrane substrate," *IEEE Trans. Microw. Theory Techn.*, vol. 62, no. 12, pp. 3249–3254, Dec. 2014.
[18] A. L. C. Serrano, A.-L. Franc, D. P. Assis, F. Podevin, G. P. Rehder, N. Corrao, and P. Ferrari, "Slow-wave microstrip line on nanowire-based alumina membrane," in *IEEE MTT-S Int. Microw. Symp. Dig.*, Jun. 2014, pp. 1–4.
[19] D. M. Pozar, *Microwave Engineering*, 4th ed. Hoboken, NJ, USA: Wiley, 2012.
[20] M. K. Khandelwal, B. K. Kanaujia, and S. Kumar, "Defected ground structure: Fundamentals, analysis, and applications in modern wireless trends," *Int. J. Antennas Propag.*, vol. 2017, pp. 1–22, 2017. [Online]. Available: https://www.hindawi.com/journals/ijap/2017/2018527/
[21] H. Moody, "The systematic design of the Butler matrix," *IEEE Trans. Antennas Propag.*, vol. AP-12, no. 6, pp. 786–788, Nov. 1964.
[22] T.-Y. Chin, J.-C. Wu, S.-F. Chang, and C.-C. Chang, "A V-band 8 × 8 CMOS Butler matrix MMIC," *IEEE Trans. Microw. Theory Techn.*, vol. 58, no. 12, pp. 3538–3546, Dec. 2010. [Online]. Available: https://ieeexplore.ieee.org/document/5629461
[23] W. Sun, X. Rao, G. Su, L. Sun, C. Shu, and X. Chen, "A miniaturized wideband 4×8 Butler matrix for beamforming in millimeter-wave applications," *IEEE Trans. Microw. Theory Techn.*, vol. 71, no. 10, pp. 4588–4599, Oct. 2023. [Online]. Available: https://ieeexplore.ieee.org/document/10102343
[24] Y. Yang, W. Luo, and C. Zhang, "A novel millimeter wave multiple beam antenna with SIW Butler matrix," in *Proc. IEEE Int. Conf. Comput. Electromagn. (ICCEM)*, Mar. 2019, pp. 1–3.
[25] N. T. Tuan, K. Sakakibara, K. Iwasa, T. Okunaga, N. Kikuma, and Y. Sugimoto, "Millimeter-wave Butler matrix beamforming circuit using finline in double-layer dielectric substrate," *IEEE Open J. Antennas Propag.*, vol. 1, pp. 579–589, 2020. [Online]. Available: https://ieeexplore.ieee.org/document/9217577
[26] K. Tekkouk, J. Hirokawa, R. Sauleau, M. Ettorre, M. Sano, and M. Ando, "Dual-layer ridged waveguide slot array fed by a Butler matrix with sidelobe control in the 60-GHz band," *IEEE Trans. Antennas Propag.*, vol. 63, no. 9, pp. 3857–3867, Sep. 2015. [Online]. Available: https://ieeexplore.ieee.org/abstract/document/7119566
[27] M. Farahani, M. Akbari, M. Nedil, A.-R. Sebak, and T. A. Denidni, "Millimeter-wave dual Left/Right-hand circularly polarized beamforming network," *IEEE Trans. Antennas Propag.*, vol. 68, no. 8, pp. 6118–6127, Aug. 2020. [Online]. Available: https://ieeexplore.ieee.org/document/9067042
[28] J. Hirokawa and N. J. G. Fonseca, "Generalized one-dimensional parallel switching matrices with an arbitrary number of beams," *IEEE J. Microw.*, vol. 1, no. 4, pp. 975–988, Oct. 2021. [Online]. Available: https://ieeexplore.ieee.org/document/9546834

BRUNO M. VERONA was born in São Paulo, Brazil, in 1991. He received the Electrical Engineering and M.Sc. degrees from the Polytechnic School of the University of São Paulo, Brazil, in 2013 and 2021, respectively. He is a Researcher with the Institute for Technological Research (IPT) and is currently the Head of the Micro-manufacturing Laboratory (LMI). His research interests include microfluidic systems, miniaturization of sensors and actuators, RF MEMS, and microfabrication processes.

ELIGIA SIMIONATO (Student Member, IEEE) is currently pursuing the bachelor's degree in electronics and telecommunications engineering with the São Paulo State University's School of Engineering of São João da Boa Vista (FESJ-UNESP), São João da Boa Vista, São Paulo, Brazil. She is also a Student-Researcher with the Center for Advanced and Sustainable Technologies (CAST). Her research interests include modeling and optimizing millimeter-wave devices and antennas using electromagnetic simulation software.

GUSTAVO PALOMINO received the B.S. degree in electronics engineering from Universidad Nacional de Ingenieria, Lima, Peru, in 2014, and the M.S. degree in electrical engineering from the State University of Campinas, São Paulo, Brazil, in 2020. He is currently pursuing the Ph.D. degree in electrical engineering with the University of São Paulo, São Paulo, Brazil, conducting research in millimeter wave devices based on nanowire membrane and in millimeter wave packaging. At the end of the undergraduate study, he joined the National Institute of Research and Training in Telecommunications, Peru, working in electronics engineering, with a focus on microwave devices.

IVAN ALDAYA (Member, IEEE) received the degree in telecommunications engineering from Universidad Pública de Navarra and the Ph.D. degree in information and communications technologies from Instituto Tecnológico y de Estudios Superiores de Monterrey. During the Ph.D. study, he carried out research internships with Universitã di Bologna and École Nationale Supérieure des Telecommunications. After the Ph.D. study, he was a Postdoctoral Researcher first with the Department of Optical Communications, Instituto Tecnológico y de Estudios Superiores de Monterrey and then with Gleb Wataghin Institute of Physics, University of Campinas. He is currently an Assistant Professor with São Paulo State University and also a part of the Center for Advanced and Sustainable Technologies (CAST) Research Group. His main research areas are optical communications (including radio over fiber systems and digital coherent systems) and the application of artificial intelligence to optimize integrated photonic devices and antennas.

RAFAEL A. PENCHEL (Member, IEEE) received the B.Sc. degree in telecommunications engineering and the M.Sc. degree in electrical engineering from the Federal University of Minas Gerais, in 2006 and 2009, respectively, and the Ph.D. degree in electrical engineering from the Pontifical Catholic University of Rio de Janeiro, in 2014. He was a Postdoctoral Researcher with the National Institute of Communications of Brazil (Inatel) in 2015, where he developed new techniques for the synthesis of reflector antennas for millimeter waves. Currently, he is an Assistant Professor with São Paulo State University (UNESP) and also a part of the Center for Advanced and Sustainable Technologies (CAST) Research Group. His research interests include the design, analysis, and fabrication of microwave and millimeter wave antennas and devices using modern technologies, such as the nanowire membrane and additive manufacturing process.

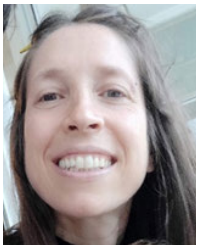

ARIANA L. C. SERRANO (Member, IEEE) was born in São Paulo, Brazil, in 1976. She received the Electrical Engineering and M.Sc. degrees from the Polytechnic School of the University of São Paulo, Brazil, in 1999 and 2007, respectively, and the Ph.D. degree from the University of São Paulo, Brazil, and the Grenoble Institute of Technology (INPG), Grenoble, France. She was a Postdoctoral Researcher with the Laboratory IMEP-LAHC, Grenoble, from 2011 to 2012, where she initiated the development of slow-wave devices on millimeter-wave frequencies. She has professional experience in telecommunications systems (with Nortel Networks) and in development of RF hardware, specially radars and satellites (with Thales/Omnisys, from 2003 to 2008). She is currently an Associate Professor with the University of São Paulo. Her current research interests include planar microwave and millimeter-wave devices, reconfigurable and tunable circuits, including modeling and characterization and slow-wave devices. She is an Associate Editor of the IEEE Microwave and Wireless Components Letters and holds three patents.

GUSTAVO P. REHDER was born in São Paulo, Brazil, in 1979. He received the B.S. degree in electrical engineering from Arkansas State University, Jonesboro, USA, in 2003, and the M.S. and Ph.D. degrees in electrical engineering from the University of São Paulo, São Paulo, in 2005 and 2008, respectively.

Currently, he is an Associate Professor with the Department of Electronic Systems, Polytechnic School of the University of São Paulo. He is also a Researcher with the Laboratory of Microelectronics (LME) and co-responsible of the Center of Millimeter Waves. His research interests include the development of tunable millimeter wave devices based on new technologies, such as MEMS and nanowire membrane.